# MRI-Guided Prostate Motion Tracking using Multislice-to-Volume Registration

by

Hadi Tadayyon

A thesis submitted to the
Department of Electrical and Computer Engineering
in conformity with the requirements for
the degree of Master of Applied Science

Queen's University
Kingston, Ontario, Canada
July 2010

# Abstract

MRI-guided prostate needle biopsy requires compensation for organ motion between target planning and needle placement. Two questions are studied and answered in this work: is rigid registration sufficient in tracking the targets with a maximum error of 3 mm (smaller than average prostate tumor size) and how many intra-operative slices are required to obtain this accuracy? We developed rigid and deformable multislice-to-volume registration algorithms for tracking the biopsy targets within the prostate. Three orthogonal plus additional transverse intra-operative slices were acquired in the approximate center of the prostate and registered with a high-resolution target planning volume. Simulated intra-operative data, phantom data, and MRI-guided robotic prostate biopsy data were used to assess tracking accuracy. Registration tests on simulated intra-operative data with 3, 4, and 5 slices were performed to evaluate the effect on registration error and time. Results: Using three orthogonal slices provides sufficient accuracy. Convergence test results on phantom images demonstrated 100% success rate for initial misalignment of 5mm. Average registration errors for the patient data were 2.55mm and 2.05mm for the rigid and deformable algorithms, respectively. The algorithm was able to capture rigid biopsy target displacements of maximum 8mm and non-rigid displacements of maximum 1.5mm. Rigid tracking appears to be promising. Deformable registration does not seem warranted.

# Acknowledgments

First I would like to thank my supervisor, Dr. Gabor Fichtinger, and research staff member András Lassó, for their dedicated mentorship throughout my research. The National Institute of Health (U.S.A.) also played a big role in my research - providing the funding. We would like to thank the staff at the U.S. National Cancer Institute for providing clinical MRI data and Princess Margaret Hospital for providing phantom MRI data. I would also like to thank Siddharth Vikal for providing research related consultations and helping me with technical problems.

# Glossary of Terms

| | |
|---|---|
| **2D** | 2-dimensional |
| **CC** | Cross-correlation |
| **CMA-ES** | Covariance Matrix Adaptation Evolutionary Strategy |
| **Core** | A sample tissue obtained from a biopsy |
| **CT** | Computed Tomography |
| **DICOM** | Digital Imaging and Communications in Medicine is a file format and a medical directory structure to facilitate access to the images and related information stored on media that share information. |
| **DOF** | Degrees of Freedom |
| **DRE** | Digital Rectal Exam |
| **FEM** | Finite Element Model |
| **Fiducial** | See landmark |
| **FRE** | Final Registration Error |
| **GPU** | Graphics Processing Unit |
| **Ground Truth** | A known quantity which can be used against an experimental result to assess its accuracy |

| | |
|---|---|
| **Intraoperative** | During operation; in biopsy, immediately after a needle insertion |
| **IRE** | Initial Registration Error |
| **ITK** | Insight Segmentation and Registration Toolkit is an open-source library of C++ classes dedicated to performing image processing (especially medical image processing). Available at www.itk.org. |
| **Landmark** | A feature or a set of features that appear in both fixed and moving images to be registered |
| **MI** | Statistical Mutual Information |
| **MRI** | Magnetic Resonance Imaging |
| **OR** | Operating Room |
| **Phantom** | A tissue/organ simulating material used for surgical training |
| **Post-needle Volume** | Equivalent of intraoperative volume; see intraoperative |
| **Pre-needle Volume** | Anatomical reference volume; preoperative volume; target planning volume |
| **Preoperative** | Before operation |
| **PSA** | Prostate Specific Antigen |
| **RAS** | Right-Anterior-Superior anatomical coordinate system |
| **RF** | Radio-frequency |
| **SDE** | Surface Distance Error |
| **SNR** | Signal-to-Noise Ratio is a measure of corruption of a signal by noise, expressed as a power ratio: $SNR = \frac{P_{signal}}{P_{noise}}$ |

| | |
|---|---|
| **SSD** | Sum of Squared Differences |
| **Tracking Slices** | Intraoperative slices that are used to form the intraoperative sparse volume |
| **TRUS** | Transrectal Ultrasound |
| **US** | Ultrasound |
| **VOI** | Volume of Interest |
| **Voxel** | A volume element of a three-dimensional digital image (analogous to a pixel in a two-dimensional digital image) |

# Table of Contents

# List of Tables

# List of Figures

# Chapter 1

# Introduction

Prostate cancer continues to be a worldwide health problem and the most common type of cancer among men in the United States. In the year 2009, prostate cancer accounted for 25% of all the diagnosed cancers. Between the years of 1996 and 2004, an estimated 91% of newly diagnosed prostate cancer cases were found to be terminal and had average survival of 5 years [1]. There are two commonly used prostate screening techniques: the Prostate-Specific Antigen (PSA) Test and Digital Rectal Examination (DRE). The PSA concentration in the blood indicates the probability of the existence of a tumor in the prostate. In a DRE, the physician checks for problems with the prostate using a gloved hand to detect abnormalities such as enlargement or irregularities in the prostate. In the event of finding elevated PSA level and abnormal DRE result, the physician may recommend a prostate biopsy for a definitive diagnosis. In a prostate biopsy, an oncologist extracts tissue samples of the prostate by driving a biopsy needle into the prostate gland through the rectal wall (transrectal) or through the perineum (transperineal). The extracted samples are then forwarded to the pathology department for diagnosis. A biopsy procedure requires image guidance

in planning and needle placement. Ultrasound (US) guided core needle biopsy is the current gold standard imaging modality. However, currently practiced procedures use 2D intra-operative US images which make it difficult for the physician to reach the target due to a lack of a constant visual reference, although volume based tracking methods have been proposed[2]. Lack of 3D guidance and poor image quality have resulted in 10-25% false negative biopsies [3]. Magnetic Resonance Imaging (MRI) is increasingly becoming the modality of choice in prostate biopsy [4] and interventional imaging due to its high soft-tissue contrast and radiation-free environment. MR imaging of the human prostate is especially of high interest in biopsy planning due to the clear prostate contour[5] and high sensitivity for detecting prostate tumors[6].

## 1.1 Motivation

A workflow of the MRI-guided transrectal robotic prostate biopsy currently in clinical trials is illustrated in Figure 1.1. A diagnostic quality MR volume of the patient's pelvis is acquired before the biopsy session, which the physician studies to determine the biopsy target locations. This volume is referred to as the target planning volume. In the biopsy session, another MR volume is acquired immediately before each needle insertion to confirm biopsy locations, known as the pre-needle insertion volume. After proper needle adjustments are made, the needle is inserted, the core is obtained, and the needle is retracted. A post-needle insertion MR volume is acquired to verify needle placement, known as the post-needle insertion volume. Physicians have encountered a major problem in this procedure: the needle puncture marks in the post-needle insertion image do not match with the originally planned biopsy positions defined in the target planning volume. This is due to prostate motion and deformation between

pre-needle and post-needle insertion. This clinical observation has been quantified by Xu *et al.* [7] in a recent longitudinal study of MRI-guided transrectal prostate biopsy cases accrued over several years. An average biopsy target displacement of 5.4mm was found. Many of these biopsy inaccuracies, which were realized post-intervention, have led to repeat biopsy. Repeat biopsies incur extra costs to the health care provider and increased health complications to the patient. This creates the need for a system to track the prostate position throughout the biopsy procedure.

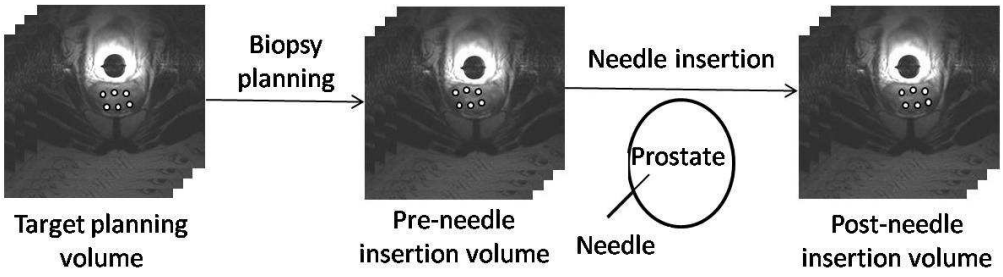


Figure 1.1: The clinical workflow of MRI-guided transrectal robitic prostate biopsy

## 1.2 MRI-based Prostate Tracking Techniques

Multislice-to-volume registration is the concept of registering a volume (often composed of many slices) to several slices of the same or lower resolution. In image-guided procedures, slices are usually acquired intra-operatively and the volume is acquired prior to operation. In the context of US, 3D-3D registration methods for prostate motion compensation have been proposed by Karnik *et al.* [8] and Baumann *et al.* [2]. Unfortunately, this technique cannot be used for MRI because volumetric MR imaging is a prohibitively long procedure for real-time motion tracking applications.

Orthogonal 2D-3D registration methods also have been proposed [9], however, due to the poor visibility of the contour and regions within the prostate gland, identifying biopsy positions is a difficult task in US images. Due to the noisy nature of the US modality (such as partial object occlusions and imperfections), intensity-based registration may not deliver the desired results. In such cases, some groups exploit a speckle-based registration technique. In US imaging, speckles are patterns formed by the interference of backscattered echoes produced by ultrasonic scatter of different mediums. Speckles display a unique pattern in a given region, serving as a suitable feature for registration. For instance, Song *et al.* [10] was able to recover myocardium deformation by speckle-based registration of 3D echocardiography. The assumption is that as the myocardium moves from one frame to another, the speckles follow the motion. Using the Rayleigh noise model and a set of coherent motion equations developed for speckle, registration was performed by finding the maximum similarity of the speckles rather than intensities. Although speckle-based tracking has proven to be effective and robust to noise in US [10], speckle is non existent in MR images. For the higher-end MRI systems (1.5T field strength or more) such as one used in our clinical trials, the images have a high signal-to-noise ratio (SNR), and intensity-based registration can be performed on them with reasonable accuracy.

In the context of CT and fluoroscopy, motion tracking algorithms for organs other than the prostate have been proposed, such as pulmonary lesions in the lung [11]. In this method, 2D fluoroscopy images of the lung are registered to the preoperative 3D CT volume to recover lesion motion. With the assumption of local rigidity, the texture-rich region containing the target lesion is used for registration. Although CT or fluoroscopy cannot be used for tracking the prostate as it does not appear

in the images, the ideas of local rigidity and texture mapping in this paper formed the foundation of our proposed tracking method, which will be covered in detail in section 2.4. In addition to the high SNR, the rich-texture prostate imaging capability of MRI makes it a suitable modality for intensity-based registration.

MRI-based tracking is a relatively new area of research which has branched into two potential methods: radio-frequency (RF) signal based tracking and intensity based tracking. In RF signal based tracking, the subject is scanned using a custom designed imaging sequence before and after motion. Translational motion information is then computationally derived from the resulting echo of the RF coil. Hata *et. al.* [12] developed an intra-operative MRI registration algorithm using projection profile matching of the RF echo. The algorithm was reported to be fast and semi-real time. The drawbacks of this technique are twofold, First, 3D motion compensation has not been achieved (only 2D motion can be recovered currently). Second, this technique depends on custom MR sequences and access to the MR machine to control the timing and pose of tracking scans. Such technologies are not widely available for average care facilities and cannot be considered as clinically practical. A clinically practical solution to the prohibitively long volume acquisition time and unavailability of custom scanning sequences is multislice-to-volume registration. This technique wraps around the idea of registering intraoperative slice images to the preoperative volume image to recover subject motion. Intraoperative volume acquisition time is saved by using a preoperative reference volume acquired prior to the intervention and pre-calibrating the surgical tool(s) to this volume. In the case of transrectal prostate biopsies, the surgical tool is the needle placement system (Figure 2.1). Multiple statically set slices are acquired at the scanner's isocenter, which eliminate the need for a custom MR

scanning sequence.

In the context of intensity based prostate tracking in MRI and multislice-to-volume registration, two works in particular inspired our project: Fei *et al.* [13] and Gill *et al.* [14]. Fei *et al.* developed a multislice-to-volume registration algorithm with application to radio-frequency thermal ablation of prostate cancer, in which 15 actual intraoperative prostate MRI slices from transverse, sagittal, and coronal orientations were registered to a preoperative MRI volume, respectively. The slices from each orientation were independently registered to the preoperative volume, meaning that three independent registrations were performed and the results were compared. Their algorithm featured a multi-resolution approach with an automatic restart. The automatic restart applied a random perturbation to the last transformation parameters found by the registration in order to escape from potential local extrema of the cost function and re-execute the registration process. This task is performed to increase chances of finding the global extreme of the cost function, which corresponds to the best alignment of the prostate in the input images. Random restarts tend to slow down the registration process.

The problem of local extreme traps and the inefficiency of Fei's optimization were addressed by Gill *et al.*. They eliminated the need for restarting the routine by performing a multi-resolution registration alone on a volume of interest (VOI), and incorporated transverse and sagittal slices centered at the prostate, which were formed into a simulated intraoperative volume. Multi-resolution registration involves a multi-step registration process in which registration starts at downsampled images and refines the transformation parameters as the the image resolution is increased. In an earlier paper [15], we improved on Gill's performance in a rigid scheme in two ways.

First, we used three orthogonal intraoperative slices rather than two. Second, we used the Insight Toolkit (ITK, www.itk.org) for the registration framework as opposed to MATLAB (MATLAB, wwww.mathworks.com), which offers higher computational performance by utilizing a more efficient memory allocation scheme. Despite its speed advantage, like earlier works, our algorithm did not consider deformations.

## 1.3 Objectives

Our objective is to develop rigid and deformable multislice-to-volume registration techniques to compensate for patient motion in MRI-guided transrectal biopsy procedure. **Six degree-of-freedom motion** (translations along and rotations about x, y and z axes) as well as **deformable displacement field** must be recovered. In the scope of prostatic needle placement, a registration error less than **3 mm** is considered to be sufficiently accurate as it is comparable to the diameter of a standard biopsy needle and smaller than the diameter of the clinically significant tumor which is about 4 mm [16]. The objective of tracking is to ascertain current prostate position prior to insertion of the biopsy needle. Tracking is requested by the physician and executed by the operator through the console, so the requirement for speed is timely response to the physician's requests. This timely response may be allowed up to **1 minute**.

We propose to position the prostate in the scanner's isocenter and acquire multiple statically set slices in this position. It is hypothesized that full six degree-of-freedom (DOF) motion of the prostate can be recovered through the registration of a target planning MR volume and multiple MR slices acquired immediately before and after needle insertion. The tracking slices are acquired with ordinary anatomical imaging

sequences through the scanner's console. This approach is affordable, as slice acquisition takes only a few seconds and is available on any commercial MRI scanner without restriction.

## 1.4 Contributions

Our present contributions are threefold:

- Development of deformable prostate tracking scheme using preoperative volume MRI and intraoperative slice MRI. To the knowledge of the author, advisor, and collaborators, this approach with the mentioned specifications has not been attempted before, though volume-to-volume approaches have been proposed [17].

- Elimination of the need for random restarting and multi-resolution scheme that hampered earlier works [13][14]. As previously mentioned, random restarts and multi-resolution registration reduce temporal performance. We took advantage of decoupled optimization which improved temporal performance. Decoupled optimization is a technique whereby translations are first optimized and then the results are used as initial center of rotation to optimize rotations. More about decoupled optimization will be covered in section 2.5.

- Analysis of the performance on simulated intraoperative MRI, phantom MRI, and clinical MRI-guided prostate biopsy data. Earlier groups reported validation only on simulated or patient data, and lacked phantom study [13][14].

As we quoted in our recent paper [18], "The straightforwardness of our approach must not belie the investment of creative efforts needed to make it a workable clinical tool,

despite the availability of several underlying algorithmic components developed by others in synergistic problems. We constructed an intuitive, practical, and inexpensive solution for a pressing clinical problem. Our solution blends seamlessly with the current MRI scanner install base and workflow, so it could be translated to patient care in a reasonable timeframe with minimal cost."

## 1.5 Organization of Thesis

We have introduced the various motion tracking techniques used in MRI-guided interventions in this chapter, in which the shortcomings of the current technologies have been described, and presented our motivation and contribution which overcome these shortcomings. In chapter 2: Methodology, we will describe the image preprocessing and workflow of the tracking algorithm, feature selection for accuracy evaluation, registration components, biopsy targets, and data used for the experiments. In chapter 3, rigid and deformable registration errors found from the simulation, phantom, and retrospective clinical studies are presented along with their registration time. Concluding remarks and future work are discussed at the end.

# Chapter 2

# Methods

## 2.1 Workflow

The goal is to develop a rapid and accurate registration of a high-resolution target planning MR volume with static MR slices acquired immediately before and after needle insertion. The clinical setup we consider is such that the patient is in prone position, a transrectal robotic probe is inserted into the rectum, and the patient is sent into the bore. An initial survey MRI is performed in order to check the position of the probe relative to the prostate. If necessary, the probe is repositioned and the patient is sent back into the bore. Once the desired position of the probe has been confirmed with survey MRI, a set of high-resolution transverse MR slices are acquired and compounded into a volume for target planning. This target planning "pre-needle volume" serves as anatomical reference for the subsequent slice registrations. A side view of the MRI-compatible needle placement robot developed by Krieger *et al.* [19] is shown in Figure 2.1. Patient MRI data for our registration tests were obtained from clinical trials conducted using this device.

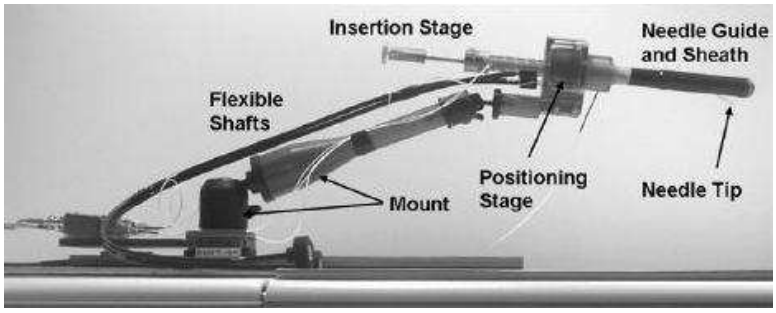


Figure 2.1: Side view of the MRI-compatible needle placement robot developed by Krieger *et al.*

Our tracking algorithm was validated on three types of data - simulated patient, phantom, and retrospective patient data. Detailed explanation of these data groups will be covered in section 2.7. The input formatting pipelines for the three data types are illustrated in Figures 2.2, 2.3, and 2.4. The pre-processing stage of our algorithm must place the slices in the correct position and orientation in a sparse volume. The slice origin and direction cosines read from the DICOM tags are used to resample the slices into a sparse volume. The bounding box of the prostate is defined as the volume of interest in the sparse volume. To form the simulated data, initial random deformation field followed by rigid perturbation were computationally applied to the pre-needle patient volume to form a simulated post-needle volume, as shown in Figure 2.2. Detailed explanation of how the deformation field and rigid perturbations were created are provided in section 2.7.1.

An intensity-based registration method was used to compensate for prostate motion. The algorithm was implemented from the registration framework of ITK, which

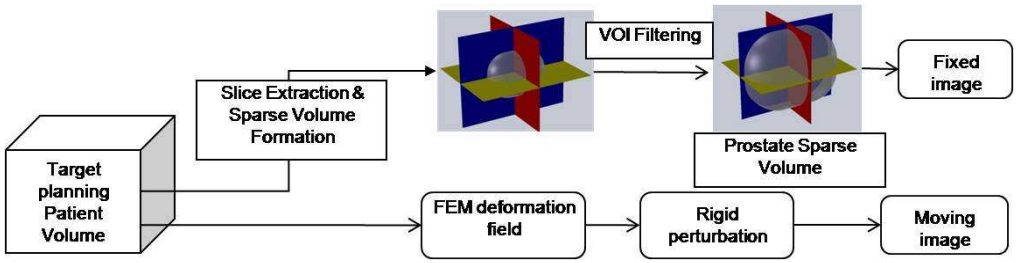


Figure 2.2: Preprocessing pipeline for simulated data

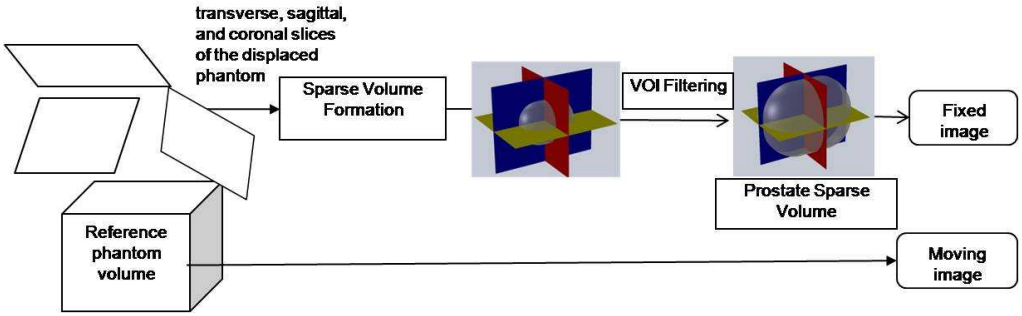


Figure 2.3: Preprocessing pipeline for phantom data

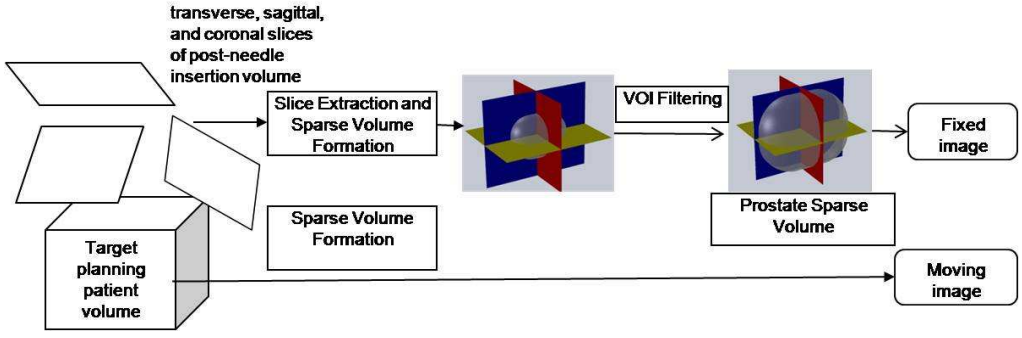


Figure 2.4: Preprocessing pipeline for clinical data

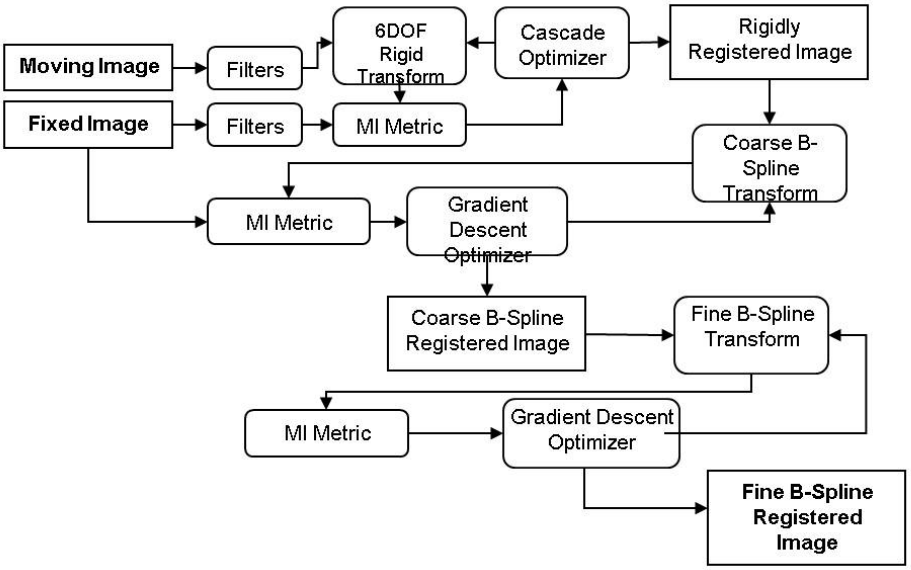


Figure 2.5: Program workflow

interconnects the registration components (selected by the programmer) and performs an iterative cost function optimization. The main registration components include fixed and moving images (inputs), metric, interpolator, transform, and optimizer. The functions of the registration components are described in sections 2.3, 2.4, and 2.5. The algorithmic concept behind the method is to find an optimum transformation matrix which best aligns the target image to the source image so as to obtain maximum overlap of a certain feature of interest. In our case, the feature of interest is the prostate. This method is referred to as intensity-based because the cost function to be optimized is a similarity metric, which attempts to find the highest match of intensities of the input images. The metric used in our case is mutual information (MI). Figure 2.5 shows the flow of the registration algorithm. The registration is performed in two stages: A rigid registration is first performed to obtain an initial

pose of the pre-needle volume, which is then non-rigidly registered to the fixed, rigid post-needle sparse volume.

## 2.2 Landmark Selection

Landmark selection is a difficult and sometimes impossible task in prostate registration problems. Depending on the imaging modality and the quality of the image, certain features can be detected. For instance, Karnik et. al [8] used calcifications in the ultrasound images of the prostate as fiducials for registration evaluation, as shown in Figure 2.6 (a). Fei *et al.* [20] used bony landmarks in the MRI prostate images (Figure 2.6(b)). However, not all images contain visible landmarks, and in most cases images that have visible landmarks are of diagnostic quality which are not available in intraoperative imaging, as was the case for [20]. In the case of [8], the calcifications, used as registration landmarks, are intrinsic fiducials which appear only in some patients. Thus, the registration experiments were limited only to patients who had calcifications. One way to evaluate registration error in the absence of landmarks is to segment the organ/tissue of interest out of the image and compute the surface distance error before and after registration. This method was chosen for the evaluation of our registration since no anatomical or external landmarks were present or detectable in our images (Figure 2.6(c)).

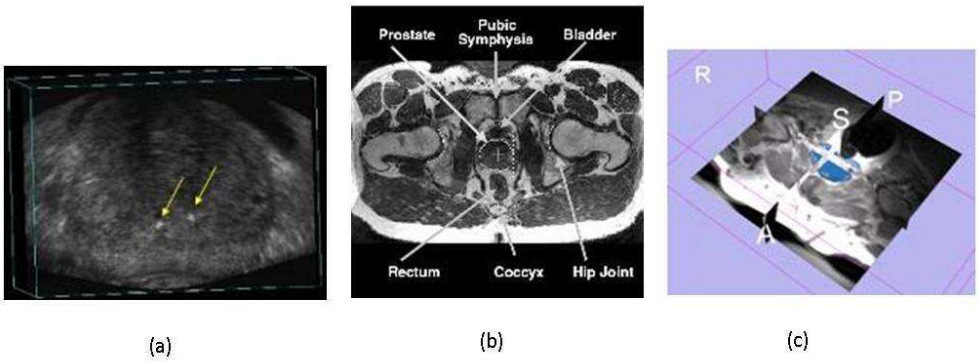


Figure 2.6: Registration features

## 2.3 Metric

In motion tracking applications where a low-resolution MRI is registered to high-resolution MRI, cross-correlation (CC) and MI are commonly used as the similarity metrics in a multi-resolution approach[13][14]. Since our algorithm performs registration at single full resolution, one similarity metric must be chosen. In order to determine which metric provides optimal results, we tested three metrics , sum of squared differences (SSD), CC, and MI by plotting each metric against the six rigid motion parameters. A sample group of plots (SSD, CC and MI) for patient 1 are shown in Figures 2.7,2.8, and 2.9. The experiment was set up such that one motion parameter was varied while keeping other parameters at the optimal position. The optimal position for patient 1 was (rx, ry, rz, tx, ty, tz) = (-0.082, 0.010, -0.011, -2.95, -9.53, -2.42). For the rotation parameters, 140 points were plotted with the origin

at the optimal value, in the range of $\pm 0.35 rad$ (20 degrees). For the translation parameters, 100 points were plotted in the range of $\pm 10 mm$. The optimal position was found by manual registration of the volumes. For the MI metric, highest similarity corresponds to the global maximum of the cost function while for the CC and SSD metrics, highest similarity corresponds to the global minimum of the cost function. Among the three metrics that were plotted, MI produced maxima which were closest to the optimal parameters.

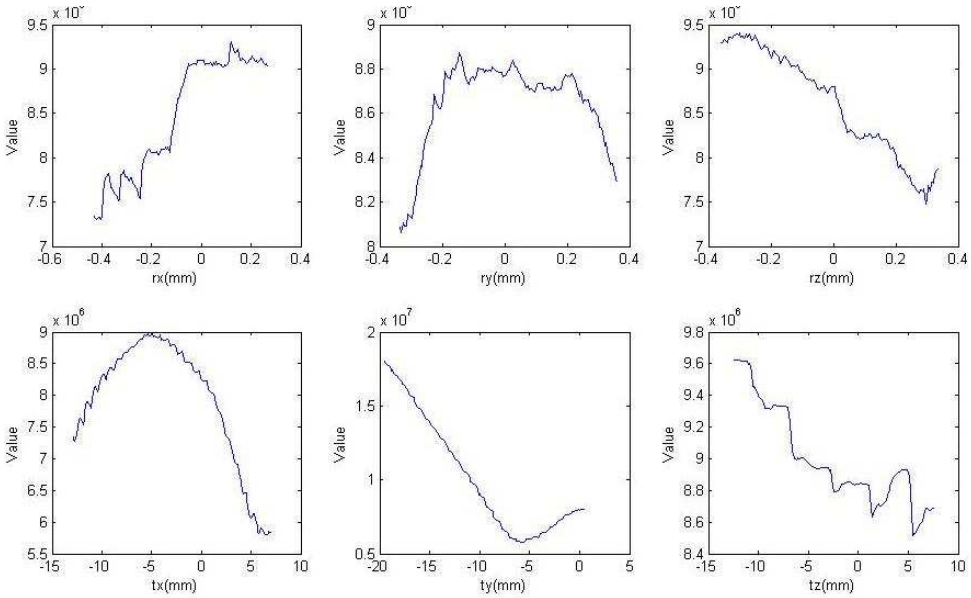


Figure 2.7: Plot of SSD metric against rotations (rx,ry,rz) and translations (tx,ty,tz) for patient 1. The metric was computed was the pre-needle volume was moved away from the optimal position relative to the fixed post-needle volume.

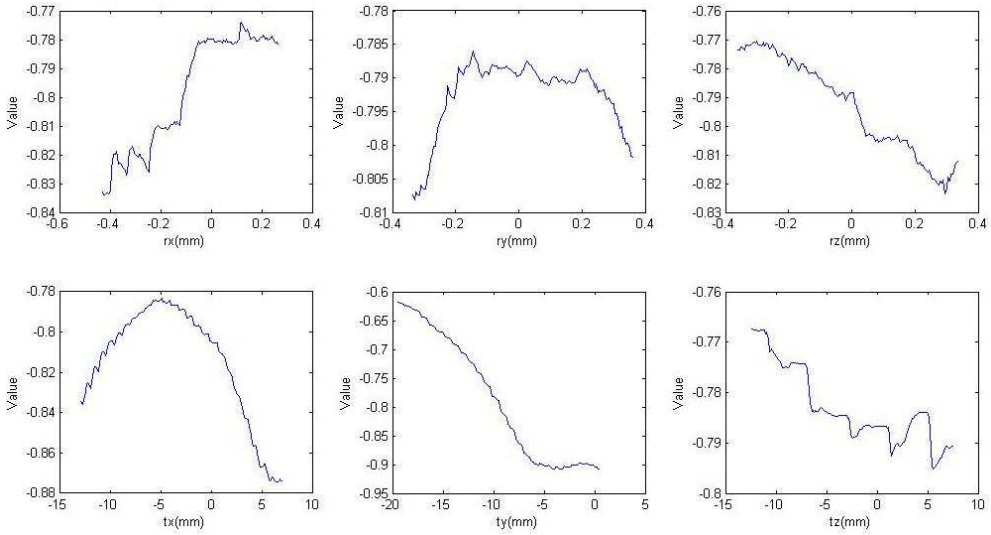


Figure 2.8: Plot of CC metric against rotations (rx,ry,rz) and translations (tx,ty,tz) for patient 1. The metric was computed was the pre-needle volume was moved away from the optimal position relative to the fixed post-needle volume.

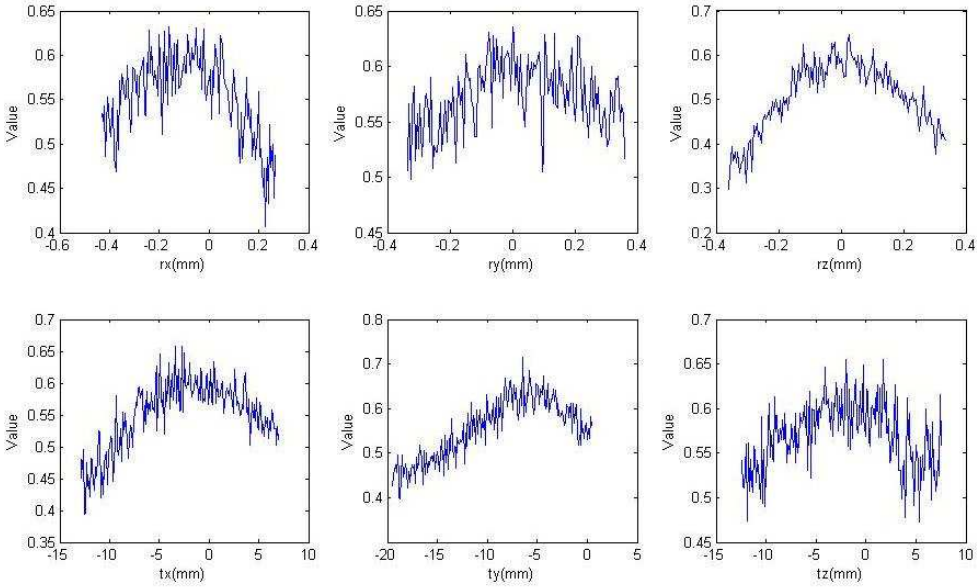


Figure 2.9: Plot of MI metric against rotations (rx,ry,rz) and translations (tx,ty,tz) for patient 1. The metric was computed was the pre-needle volume was moved away from the optimal position relative to the fixed post-needle volume.

## 2.4 Filtering and Volume-of-Interest

A VOI was defined to constrain motion to the prostate region. The rigid registration scheme assumes that the VOI undergoes rigid motion from one frame to another, meaning that the prostate is assumed to be rigid. The deformable registration scheme used the same VOI, but did not assume rigidity, to save computation time.

Once the VOI was defined, two spatial filters were applied to the VOI to enhance the prostate image. A histogram matching filter was first applied to the moving image to match the intensities of the fixed image. The moving and fixed images

were then passed through a Gaussian smoothing filter in order to obtain smooth intensity estimates for our mutual information similarity metric. Random intensity samples were drawn from the fixed image to calculate the joint probability distribution function. The size of the intensity sample population was set to 10% of the total voxel size of the fixed image. The choice of the values of the metric parameters, including smoother variance and population size, was based on trial and error. The smoother variance value was chosen as the optimal balance between smoothness of the density function (low variance) and loss of intensity modes (high variance). The population size was chosen based on the optimal balance between computational speed and accuracy of the joint probability distribution function.

## 2.5 Interpolations, Transformations, and Optimizations

The interpolator component of registration is responsible for finding the mapping of a point from the fixed image space to the moving image space at non-grid positions. In our application, linear interpolation was performed, which assumed that intensities vary linearly between non-grid positions.

Rigid transformation optimization proceeds in a cascade model, in which the translation parameters are optimized using the CMA Evolutionary Strategy (CMA-ES) [21]. The CMA-ES is an evolutionary algorithm for difficult non-linear non-convex optimization problems in continuous domain. The CMA-ES has several invariance properties. Two of them, inherited from the plain evolution strategy, are (i) invariance to order preserving (i.e. strictly monotonic) transformations of the objective

function value and (ii) invariance to angle preserving (rigid) transformations of the search space (including rotation, reflection, and translation), if the initial search point is transformed accordingly. The CMA-ES does not require a tedious parameter tuning for its application. The user is not required to tune internal parameters except the population size. Following translation, rotation is optimized by gradient descent optimization. For our application, the CMA-ES was not able to optimize a 6-DOF search space as it diverged on rotations regardless of scaling. Thus, we decoupled the translation and rotation optimizations and used the CMAES for the parameters that varied the most, i.e. the translation. The gradient descent optimizer converges quickly and accurately for parameters that have a smaller variation range, i.e. the rotations in our case. The order of optimization is key here; translation must be optimized first in order to align the center of rotation of the moving image with the geometric center of the fixed image. In cases where the prostate's center of mass is not aligned in the images, optimizing for rotation first results in further divergence from the solution.

We feed the rigidly registered pre-needle volume to a deformable registration algorithm, which runs through a two level registration pyramid using coarse B-Spline grid (5 x 5) followed by a finer grid (15 x 15). Using a gradient descent optimizer, we search the parameter space of the B-Spline grid for the parameters that maximize the MI value.

## 2.6 Biopsy Targets

All patients underwent a sextant biopsy, in which three cores were extracted from the peripheral zone of the base, mid, and apex of the right part, and three mirrored cores on the left part of the prostate. A visualization of the RAS location of the planned biopsy targets are shown in Figure 2.10. Our algorithm must successfully track the positions of each of these targets in patient data set.

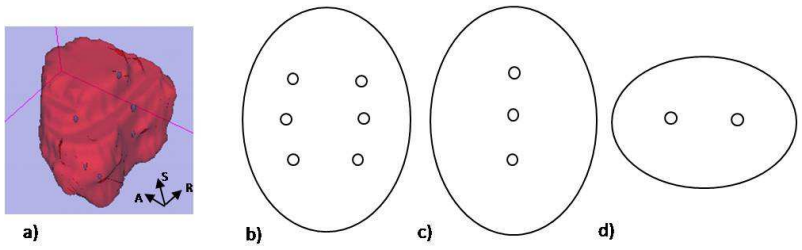


Figure 2.10: Biopsy target locations shown in isometric view (a), SR plane of view (b), SA plane of view (c), and RA plane of view (d)

## 2.7 Experimental Data

### 2.7.1 Simulated Data

In order to explore the robustness, capture range and temporal performance of our tracking algorithm on actual clinical data, we created simulated post-needle volumes using finite element (FE) modeling and rigid 6-DOF perturbation to generate realistic deformations and rigid body motions, respectively. Using a finite element analysis software application developed by Lasso *et al.* [22], we generated 20 simulated patient MR images containing the deformed prostate due to patient motion. To generate the

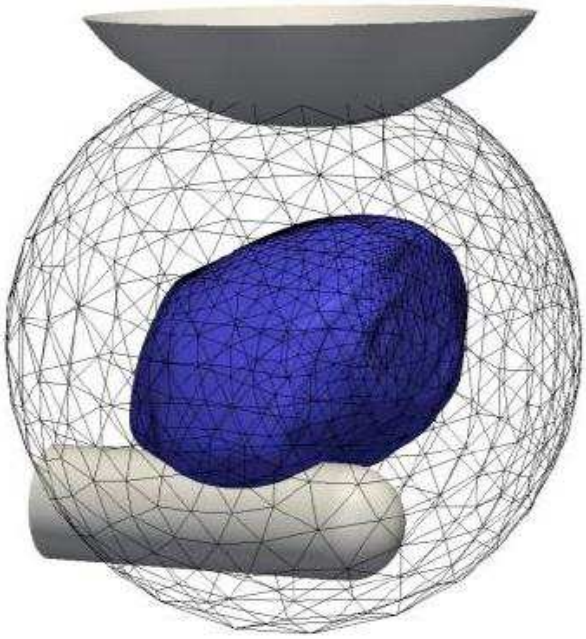

Figure 2.11: Sample geometry of the prostate (solid surface in the middle) and the body object (wireframe sphere around the prostate). Force is applied on body mesh nodes that lie within the cylindrical shape of the endorectal probe. Position of the anterior side of the body object (at the top, intersection with the solid sphere part) is fixed. Image source: Lasso *et al.*

deformable FE model of the prostate, the prostate volume was segmented out of one of the clinical patient images, from which a tetrahedral volume mesh was constructed and placed inside a spherical mesh, as shown in Figure 2.11. The spherical mesh represented the tissues surrounding the prostate, such as the bladder and urethra. To mimic the setting in which the MR images were acquired from a transrectal robot probe, the robot probe was placed inside the sphere in the form of a cylindrical mesh. Material properties of the body (spherical mesh) and the prostate were adapted from

[23]; both objects were modeled as linear elastic materials, the prostate with Poisson ratio $\nu = 0.4$ and Young's modulus E = 21 kPa, body with $\nu = 0.4$ and Young's modulus E = 15 kPa. Patient motion causes strong local pressure on the prostate by the probe. This pressure was modeled by prescribing force loads on the mid-posterior surface of the prostate. The FE solver was run on 20 cases involving different force loads (randomized) and probe positions (1D translation along rectal axis) and a ground truth deformation field was computed. The force loads were randomized in the range of $[0 < F_x < 5, -30 < F_y < 20, 0 < F_z < 2]$ N. Probe translation was randomized in the range of $-2mm < T_z < 2mm$. The coordinate system was defined such that the rectal axis was aligned with the z axis and the x axis was oriented normal to contact surface between the probe and prostate. The y axis was obtained by the right-hand rule.

Rigid perturbation was computationally applied through point transformation defined by a homogeneous transformation matrix. The transformation matrix describes the translations and rotations to be applied in a 6-DOF space. The six motion parameters (three translations and three rotations) were uniformly randomly generated for each simulation case and were constrained in the ranges of $\pm 5mm$ and $\pm 5degrees$.

### 2.7.2 Phantom Data

The phantom images were acquired from a prostate biopsy training phantom manufactured by CIRS Inc., Norfolk, VA, whose picture is shown in Figure 2.12. The prostate along with structures simulating the rectal wall, seminal vesicles, and urethra are contained in this 11.5 x 7 x 9.5 cm acrylic container. The acquisition protocol

Table 2.1: Acuisition protocol for phantom images

| | |
|---|---|
| Field Strength | 1.5T |
| Image Type | T2-weighted |
| Slice Orientation | Transverse |
| Slice resolution (mm/px) | 0.625 x 0.625 |
| Slice thickness/spacing (mm) | 3 |
| Slice Dimensions (px) | 256 x 256 |
| Number of Slices | 25 |

for the phantom images is shown in Table 2.1. The moving image was a high resolution phantom volume at the reference position and the fixed image was a sparse volume (three orthogonal slices) of the phantom after being translated or rotated from the reference position.

Figure 2.12: CIRS 053MM - Multi-modality prostate training phantom

### 2.7.3 Clinical Data

In the pursuit of a more accurate biopsy, Krieger *et al.* developed robotic assistance under MR image guidance [19]. To date, their system has been used at the U.S. National Cancer Institute in multiple clinical trials. Under ethics board approval, we have obtained five patient data sets from their studies. Each data set contained a pre-needle volume image used for target planning and a post-needle volume image used for needle placement verification. The high-resolution MRI volumes were acquired from a T2-weighted MRI transverse scan using a 1.5T GE MRI system. The target planning (pre-needle) images had resolutions of 0.78 x 0.78 x 4 mm/pixel for patient 1, 0.625 x 0.625 x 3mm/pixel for patient 2, and 0.55 x 0.55 x 3 mm/pixel for patients 3, 4, and 5. The intraoperative images had resolutions of 0.78 x 0.78 x 4 mm/pixel for patient 1, 0.625 x 0.625 x 3 mm/pixel for patient 2, 0.85 x 0.85 x 3mm/pixel for patients 3 and 4, and 0.94 x 0.94 x 3mm/pixel for patient 5. Their slice dimensions were 256 x 256 pixels for all patients. The acquired volumes varied from 16 to 25 transverse slices. We extracted three orthogonal slices from each post-needle volume, centered in the prostate. As true sagittal and coronal slices were not available, they were obtained by interpolation between the transverse image slices.

# Chapter 3

# Results

## 3.1 Simulated Registration Tests

In order to explore the robustness, capture range and temporal performance of our rigid algorithm on actual clinical data, we created simulated post-needle volumes using finite element modeling and rigid transformation to generate realistic deformations and rigid body motions, respectively. In these tests, the fixed image was a sparse volume of the pre-needle patient image. A software generated deformation field was applied to the full pre-needle volume by the method described in section 2.7.1. We applied 5 mm translation and 5 degree rotation to the deformed volume on all axes and attempted to recover the introduced biopsy target displacement. In order to assess whether three tracking slices are sufficient in estimating the out-of-plane deformation, registration tests were run on N (number of tracking slices) = 3, 4, and 5. Slices were added normal to the superior-inferior axis (transverse slices) positioned such that they bisected the prostate's superior and inferior halves. 20 registration tests were performed for each value of N, totaling the number of registrations to 60.

The results are summed up in Table 3.1. Registration error ($\epsilon$) was defined as the Euclidean distance between the ground truth points and the corresponding registered points averaged over the prostate volume of interest, as expressed in equation 3.1. L,M, and N represent the dimensions of the prostate volume of interest.

In Table 3.1, N represents the number of slices, $\epsilon_d$ and $\epsilon_r$ represent deformable and rigid errors as defined by Equation 3.1, where $P_{REG}(x, y, z)$ is the rigidly registered point for $\epsilon_r$ and non-rigidly registered point for $\epsilon_d$. Success rate (r) was defined as the percentage of registration tests that resulted in a registration error less than 3mm. Four of the 20 trials which had initial mean prostate deformation of more than 1.5mm were discarded from the results as they were outside of the algorithm's non-rigid capture range. Plots of initial error vs. final rigid and deformable registration errors for N=3, 4, and 5 are shown in Figures 3.1, 3.2, and 3.3. Initial error was defined as the mean distance between the original points in the preoperative (reference) volume and the corresponding points transformed by ground truth displacement (FEM and rigid perturbation). The rigid capture range of the algorithm for the simulated data was found to be 8mm.

$$\epsilon_{sim} = \frac{\sum_{x=0}^{L}\sum_{y=0}^{M}\sum_{z=0}^{N} |P_{GT}(x, y, z) - P_{REG}(x, y, z)|}{LMN} \tag{3.1}$$

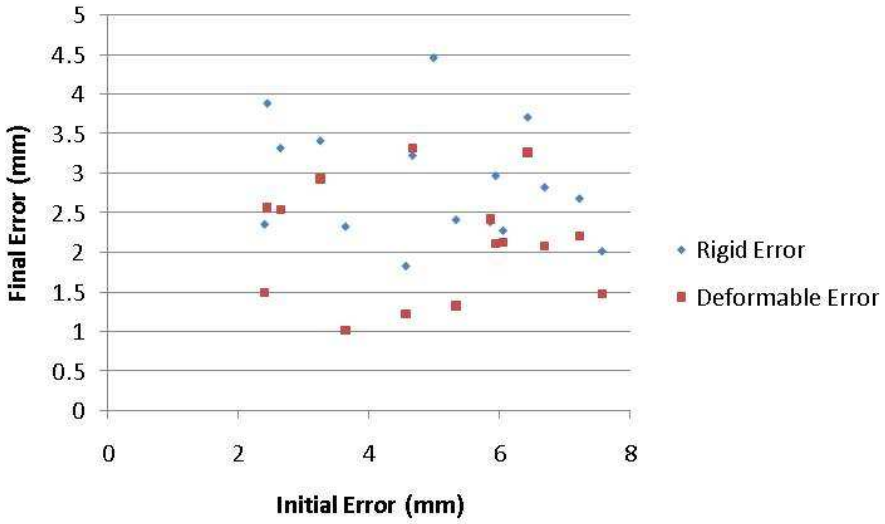


Figure 3.1: Plots of initial error vs. final rigid and deformable errors for N = 3

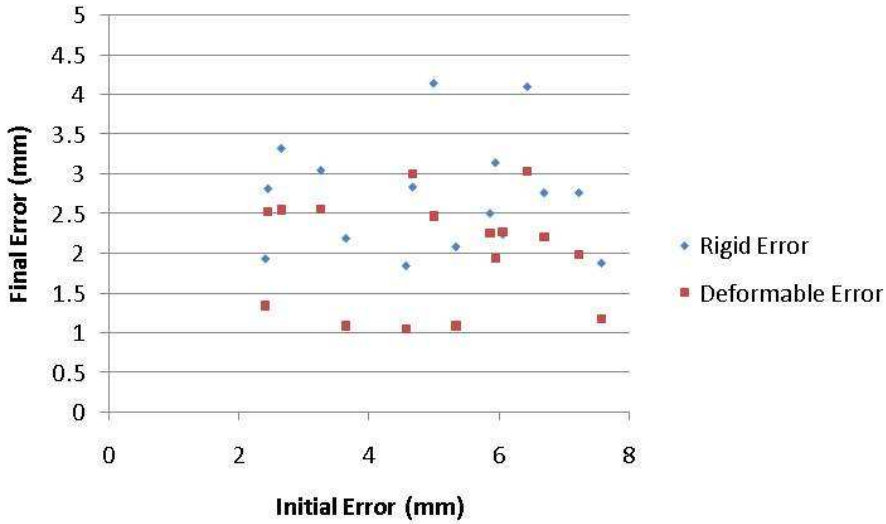


Figure 3.2: Plots of initial error vs. final rigid and deformable errors for N = 4

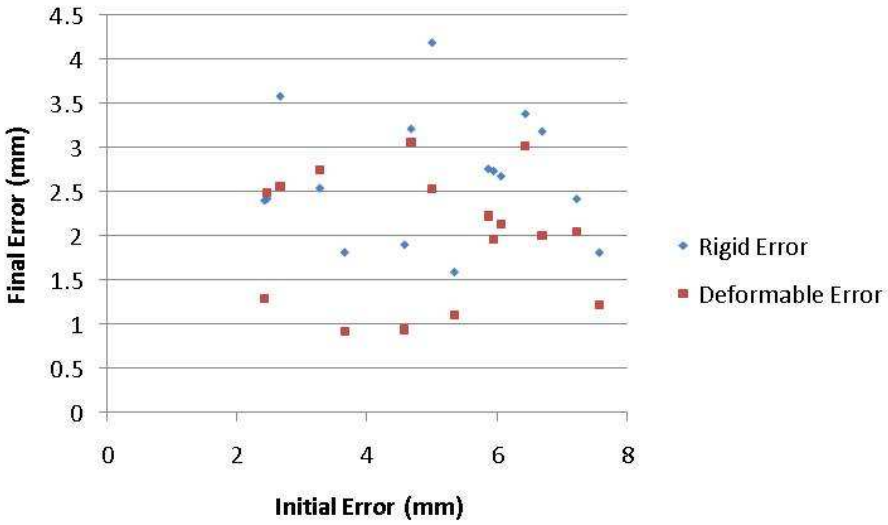


Figure 3.3: Plots of initial error vs. final rigid and deformable errors for N = 5

Table 3.1: Registration errors (deformable and rigid) for simulated patient registrations

| N | $\epsilon_d(mm)$ | $\epsilon_r(mm)$ | $r_d(\%)$ | $r_r(\%)$ | $\Delta t_d(s)$ | $\Delta t_r(s)$ |
|---|---|---|---|---|---|---|
| 3 | 2.19 | 2.88 | 90 | 70 | 360 | 60 |
| 4 | 2.03 | 2.72 | 95 | 75 | 810 | 100 |
| 5 | 2.02 | 2.66 | 90 | 75 | 1390 | 140 |

## 3.2 Phantom Study

The phantom study consisted of a two-phase test. The first phase was a simulation experiment, whereby the displaced volume was simulated from the reference phantom volume, in a similar manner to the patient simulation experiment, but only rigid motion study was performed. At the time the tests were performed, the non-rigid algorithm had not been developed. Registrations were performed for 75 random perturbations, using the same rigid range as the patient simulation case. This test was conducted first to evaluate the convergence range of our phantom images, for which a histogram was plotted from the test results, which is shown in Figure 3.4. The histogram shows the percentage of cases that successfully converged for a particular bin of initial registration error (IRE), where successful convergence was defined as a final registration error (FRE) of less than 0.5mm. A threshold of 0.5mm was used rather than 3mm for two reasons. First, the ground truth displacement between the reference and displaced volumes is precisely known for validation of registration accuracy, as it was computationally created. Thus, a stricter pass/fail condition can be applied for simulations. Second, all simulation cases resulted in less than 3mm error, and thus, using a threshold of 3mm would mean that all 75 tests converged, which would render the convergence histogram meaningless. It seemed intuitive to use 0.5mm as this was the average final registration error among the simulation tests and produced a more descriptive histogram.

The second phase of our phantom study involved six registration tests, each corresponding to a rigidly misaligned image of the phantom, as described in section **??**. The ground truth displacement of the phantom was only known in the physical coordinate system of the experimental setup, which was not known to us, as the images

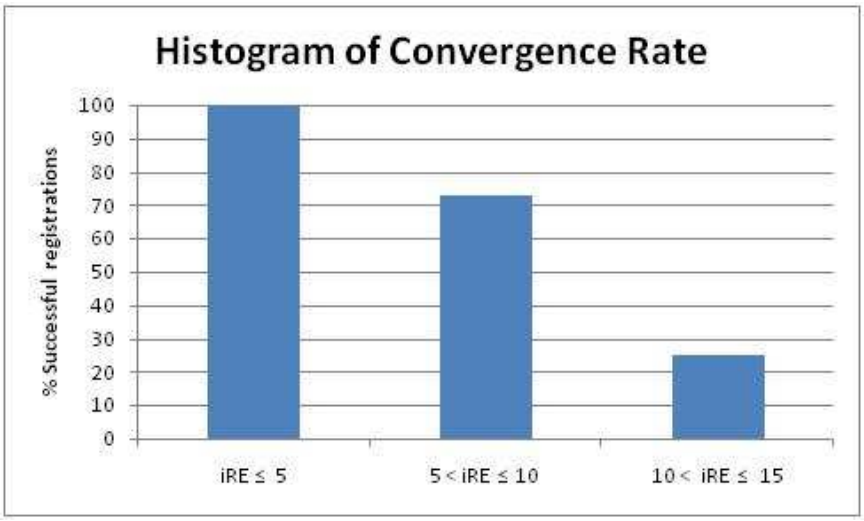


Figure 3.4: Histogram of convergence rate for phantom registrations

were acquired by a different group. Thus, our reference transformation was found by using image analysis software and manually registering the two volumes in a trial-and-error manner. Registration accuracy of the reference transform was confirmed by inspection of the overlaid source and target images. Registration error was defined as the mean Euclidean distance between reference transformed points and corresponding registered points. Equation 3.2 mathematically expresses the error measure.

$$\epsilon_{ph} = \frac{\sum_{x=0}^{L}\sum_{y=0}^{M}\sum_{z=0}^{N} |P_{REF}(x,y,z) - P_{REG}(x,y,z)|}{LMN} \tag{3.2}$$

The initial registration error (initial RE) values in Table 3.2 represent the initial misalignment based on the reference transformation found from the manual registrations we performed initially. Two of the six registration tests were excluded from the results due to a high initial registration error (16mm and 22.4mm), which resulted in

a high final registration error (4.7mm and 5.8mm). It was reasonable to dismiss these cases from the results since it is assumed that in the clinical situation, the prostate will not be displaced by more than roughly 10mm, consistent with findings of Xu *et al.* [7]. The fourth phantom test case (fourth column of table 3.2) was included in the results since the initial displacement was close to 10mm and it allowed for testing the limits of the algorithm. The mean registration error was 1.64mm and mean registration time was 42s. A checkerboard overlay of the fixed and moving phantom images before and after registration is shown in Figure 3.5 for one of the test cases. The slices shown are planes cutting through the approximate center of the prostate.

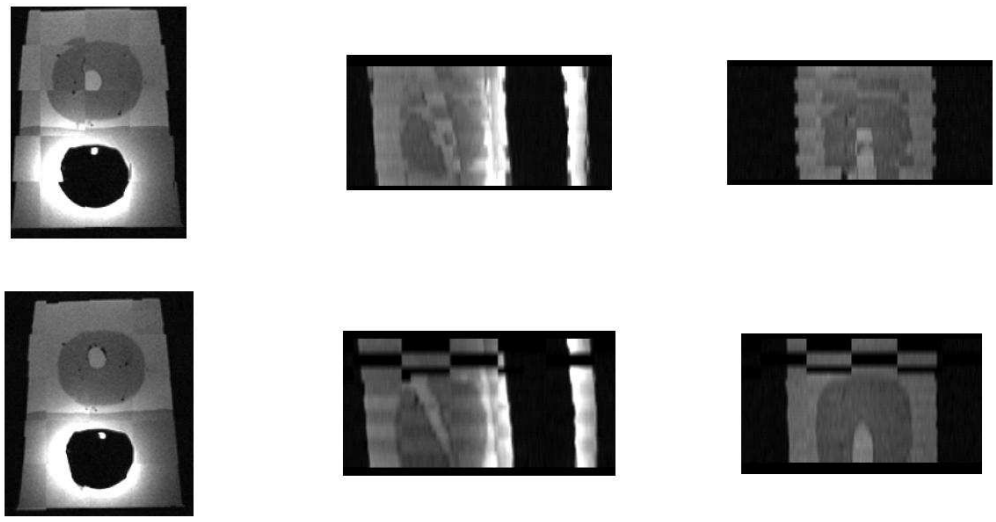

Figure 3.5: Checkerboard overlay of reference and displaced phantom volumes. Views: Transverse(left), Sagittal(Middle), Coronal(Right). Top row: Before registration. Bottom Row: After Registration.

Table 3.2: Registration Error for Phantom Registrations

| | | | | | |
|---|---|---|---|---|---|
| Initial RE(mm) | 3.50 | 5.81 | 5.97 | 12.32 | **Overall** |
| Final RE(mm) | 0.75 | 0.86 | 1.38 | 3.58 | **1.64** |

## 3.3 Clinical Study

Our retrospective clinical study involved registration tests on five biopsy patients. These patients were chosen for registration tests for two reasons. First, the images had good contrast between the prostate and the surrounding tissues. Second, we were able to test patients with normal motion (less than 5.4 mm) and those with large motion (greater than 5.4 mm). Patient motion was measured in terms of target displacement and was classified based on the average target displacement that was found by Xu *et al.* [7] (5.4 mm). Target displaced was defined as the distance between the pre-needle and post-needle insertion position of the biopsy target. As shown in Table 3.3, $D_T$ represents target displacement (mm), whose values were obtained from the findings of Xu *et al.* [7], as the patient data used were identical. Three orthogonal tracking slices (extracted) were used for registration. To validate the registrations, we segmented the prostate in both volumes and computed the mean surface misalignment after registration. We term this measure as surface distance error (SDE). For each surface, fixed and moving, the consisting points were sorted into a N x 3 array, where N is the number of points in the surface. The moving surface points were then re-sorted according to a nearest neighbor search[24] such that the distance between corresponding fixed and moving points is minimized. Equation 3.3 mathematically expresses the formulation of SDE. The results (Table 3.3) may seem surprising at first, but actually coincides with latest results in the literature contributed by Xu [7]

Table 3.3: Mean surface distance errors (mm) and standard deviations before and after registration of actual patient data sets

| | Patient No. | $D_T$ | Initial SDE | Rigid SDE | Non-rigid SDE |
|---|---|---|---|---|---|
| | 1 | 9.90 | 4.51 | 1.82 | 1.32 |
| | 2 | 7.00 | 2.23 | 2.38 | 1.93 |
| | 3 | 4.12 | 7.76 | 1.65 | 1.62 |
| | 4 | 4.36 | 4.13 | 1.88 | 1.83 |
| | 5 | 11.45 | 7.67 | 5.01 | 3.56 |
| **overall** | | **8.69** | **5.26** | **2.55** | **2.05** |
| $\sigma$ | | **2.64** | **2.15** | **1.40** | **0.87** |

and Karnik [8].

$$\epsilon_{pat} = \frac{\sum_{i=0}^{N} |P_{fixed}(i) - P_{moving_{min}}(i)|}{N} \tag{3.3}$$

The average rigid registration time was 70s for the rigid algorithm and 1000s for the deformable algorithm (includes initial rigid alignment time). The pre-needle insertion and post-needle insertion positions of the first biopsy target for patient 1 are shown in Figure 3.6. The pre-insertion position was obtained from biopsy data and the post needle position was obtained by our tracking algorithm.

The prostate surfaces before and after rigid and deformable registrations for patient 1 are shown in Figure 3.7. Note that the prostate was segmented for the purpose of validation. No segmentation was involved in the algorithm before or during registration.

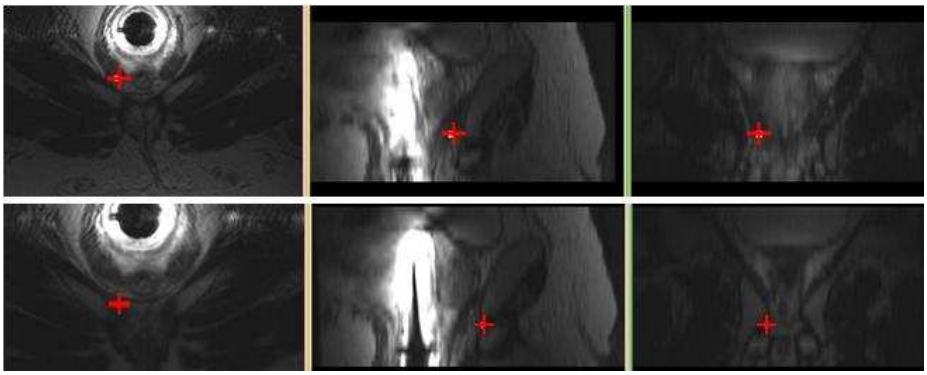

Figure 3.6: Transverse, sagittal, and coronal views of biopsy target position before needle insertion (top) and after needle insertion (bottom)

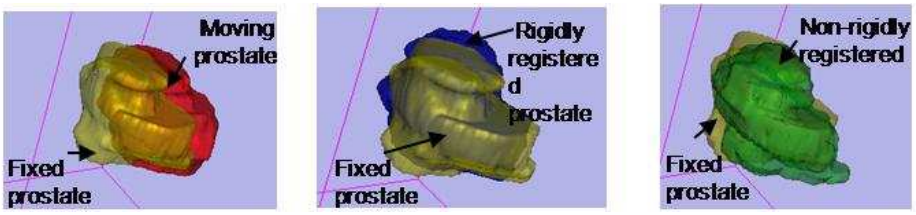


Figure 3.7: Prostate surfaces before registration (left), after rigid registration (middle), and after deformable registration (right). Just as in Table 3.3, deformable registration shows no substantial benefits.

# Chapter 4

# Discussion

## 4.1 Registration Accuracy

One major challenge of our evaluation is the fact that in clinical patient data there is no strong ground truth. As opposed to many computer assisted interventions that use fiducials to perform or evaluate registrations, there are no fiducials associated with the in-vivo prostate during a biopsy procedure. Implanting such markers for our study would involve discomfort and risk to the patient. As such, the measure of registration error for actual patient registrations for this study is based on surface misalignment (SDE). In the case of this study where an accurate ground truth is not present, point transformations cannot be used to compute error as performed by previous groups [13] since there is no reference transformation to base the error on. Absence of a ground truth also means that it is impossible to compute the target registration error (TRE), the error in estimating the motion of the target. However, Lasso *et al.* [22] assessed TRE in image-guided prostate needle placement using a FE

model of prostate. In this study, he proved that prostate deformation and segmentation error in surface-based registrations have clinically insignificant impact on TRE. Thus, it can be safely assumed that SDE is a reasonable replacement of TRE when it is not measurable.

High tracking accuracy was obtained in phantom registration tests. This was expected from a rigid motion problem. Due to time constraints, non-rigid tests were not performed on the phantom.

The relatively large variation of registration errors among the five patients is mainly due to the large time span over which the data were acquired and archived (5 years). During this time, devices (such as the probe) changed, which affected the imaging parameters such as contrast, resolution, and field of view. The time extensiveness of the legal procedure for obtaining anonymized patient data hindered the perfection of the retrospective clinical study. As a result, experiments were performed on data that was already available and the results are preliminary.

The main sources of registration error for the patient data are segmentation error and needle artifacts. Although manual segmentation is generally more accurate the automatic segmentation, the results vary between the users who segment the prostate surface. The contribution of needle artifacts to the error is probably small since it only occupies a few voxels.

Our validation work has not focused on statistical analysis of results as the number of patient data is relatively small compared to published related works. Such large scale statistical analysis has already been performed for the purpose of determining the targeting accuracy of current MRI-guided prostate biopsy procedures[7], which has prompted the need for a fast biopsy target tracking algorithm. Our algorithm's

accuracy, robustness, and time efficiency assessment is heavily dependent on phantom and simulation studies using a realistic deformable model of the prostate, putting less emphasis on studies on large population of clinical data.

The registration errors found by simulations (Table 3.1) are higher than those found by retrospective clinical tests (Table 3.3), justified by the fact that measures of error were different as explained in sections 3.1 and 3.3. Since ground truth transformation was known for the simulation data, the error was computed based on point transformation as explained in section 3.1. The error was computed over a bounding box covering the prostate. This includes voxel distance errors within the prostate as well as corners of the bounding box which are outside of the prostate. On the other hand, since the ground truth transformation for the patient data was not known, the error was measured as mean surface distance as described in section 3.3. As a result, the errors reported for the simulations consider not only the residual surface misalignment, but also how well the voxels matched within the prostate and on it's four outside corners. This explains the higher error for the simulation tests.

From the rigid and deformable registration results on limited clinical data (Table 3.3), it has been shown that only 0.5 mm improvement in SDE is achieved by the addition of a deformable registration step. A 0.5 mm error improvement is not clinically significant, which is fully in step with the latest findings of Xu [7] and Karnik [8] who suggest that their results from rigid and non-rigid intraoperative prostate biopsy registrations were not clinically significant, though statistically different. Again, clinical significance is defined in terms of average tumor size (4mm). An accuracy gain of 1.25 fold at the cost of 14 fold loss in temporal performance does not favour the deformable algorithm for clinical applications.

## 4.2 Number of Tracking Slices

The results of registration error as a function of number of tracking slices, reported in table 3.1, show that three tracking slices are sufficient in reasonably estimating the out of plane deformation of the prostate gland given the small gain in accuracy for a large loss in computational time as more slices are added. To make a clinically significant impact on accuracy and maintain fast registration speed we must use a large number of tracking slices, perhaps 10 or more, in true sagittal and coronal views, and implement the algorithm on a GPU.

## 4.3 Summary of Contributions

Rigid and non-rigid intensity based registration algorithms were developed for tracking the biopsy targets in a robotic assisted MRI-guided prostate biopsy procedure. The algorithm was tested on simulated patient MRI, phantom MRI, and clinical MRI. As observed from clinical registration results, the objective of 3 mm accuracy was fulfilled. However, the registration time slightly exceeded the objective (70 s vs 60 s). Suggestions for improving temporal performance will be discussed in section 4.4. A decoupled rigid optimization method was used, which eliminated the need for multi-resolution registration and random restarts. It was proven by simulation study that among 3, 4, and 5 tracking slices, 3 is the optimal choice for speed and accuracy. The simulated data were obtained from a realistic FE model of the prostate with accurately known ground truth rigid and non-rigid displacements. Registration results on the simulated data provided an insight into how the algorithm may behave in response a typical patient motion in a clinical scenario. The rigid algorithm does

not require random restart or multi-resolution pyramids. Rather than using coarse resolution registration results as the initial guess, translation optimization results were used. Using the data available, this method has shown more consistent results in contrast with the multi-resolution method.

## 4.4 Future work

We must stress again that our experiments were conducted with reformatted sagittal and coronal images. Under true clinical circumstances, the resolution of the sagittal and coronal tracking images will be several times higher, which will undoubtedly improve registration performance. In essence, the current tests with low-resolution non-axial slices underestimate the true power of our prostate tracking method. Also, in practice tracking slices will be acquired more often than in the data sets we received for the analysis. In real cases, we will run an additional tracking sequence immediately before needle insertion, which will divide current prostate motion and deformation errors in about half - a major improvement in target tracking performance.

Our registration time for the rigid algorithm is clinically acceptable. Deformable registration times could raise feasibility concerns, but in all we are not particularly concerned about time, because for clinical trials the registration should be ported to the GPU which then obsoletes all prior considerations.

In conclusion, results on limited clinical patient data indicate that the rigid registration is sufficient for tracking of the prostate in MRI-guided robotic biopsy. Our rigid algorithm has demonstrated convergent results for initial prostate displacements up

to 8mm. Work continues with performing target registration error studies in typical sextant and octant biopsy locations and, most importantly, moving toward a prospective clinical trial with the use of true sagittal and coronal slices.

# Bibliography

[1] A. Jemal, R. Siegel, E. Ward, and et al., "Cancer statistics, 2009," *CA: A Cancer Journal for Clinicians*, vol. 59, no. 4, pp. 225–249, 2009.

[2] M. Baumann, P. Mozer, V. Daanen, and J. Troccaz, "Prostate biopsy assistance system with gland deformation estimation for enhanced precision," *MICCAI*, vol. 5761, pp. 67–74, 2009.

[3] J. Kronz, C. Allan, A. Shaikh, and J. Epstein, "Predicting cancer following a diagnosis of high-grade prostatic intraepithelial neoplasia on needle biopsy: data on men with more than one follow-up biopsy." *The American Journal of Surgical Pathology*, vol. 25, no. 8, pp. 1079–85, 2001.

[4] B. Quesson, J. A. de Zwart, and C. T. Moonen, "Magnetic resonance temperature imaging for guidance of thermotherapy," *Journal of Magnetic Resonance Imaging*, vol. 12, pp. 525–33, 2000.

[5] M. E. Ladd, H. H. Quick, and J. F. Debatin, "Interventional MRA and intravascular imaging," *Journal of Magnetic Resonance Imaging*, vol. 12, pp. 534–46, 2000.

[6] A. Wefer, H. Hricak, D. Vigneron, F. Coakley, Y.Lu, J. Wefer, U. Mueller-Lisse, P. Carroll, and J. Kurhanewicz, "Sextant localization of prostate cancer: comparison of sextant biopsy, magnetic resonance imaging and magnetic resonance spectroscopic imaging with step section histology." *Journal of Urology*, vol. 164, no. 2, pp. 400–4, 2000.

[7] H. Xu, A. Lasso, S. Vikal, P. Guion, A. Krieger, A. Kaushal, L. Whitcomb, and G. Fichtinger, "Accuracy validation for MRI-guided robotic prostate biopsy." SPIE, 2010.

[8] V. Karnik, A. Fenster, and J. B. et al., "Assessment of registration accuracy in three-dimensional transrectal ultrasound images of prostates," vol. 7625. SPIE Medical Imaging, 2010.

[9] M. Baumann, P. Mozer, V. Daanen, and J. Troccaz, "Towards 3d ultrasound image based soft tissue tracking: a transrectal ultrasound prostate image alignment system." *MICCAI*, vol. 4792, pp. 26–33, 2007.

[10] X. Song, A. Myronenko, and D. Sahn, "Speckle tracking in 3d echocardiography with motion coherence," *Computer Vision and Pattern Recognition, 2007. CVPR '07. IEEE Conference on*, pp. 1 –7, 17-22 2007.

[11] S. Xu, G. Fichtinger, R. Taylor, and K. Cleary, "Validation of 3D motion tracking of pulmonary lesions using ct fluoroscopy images for robotically assisted lung biopsy," vol. 5744. SPIE, 2005.

[12] N. Hata, J. Tokuda, S. Morikawa, and T. Dohi, "Projection profile matching for intraoperative MRI registration embedded in MR imaging sequence," *MICCAI*, pp. 164–169, 2002.

[13] B. Fei, J. L. Duerk, D. T. Boll, J. S. Lewin, and D. L. Wilson, "Slice-to-volume registration and its potential application to interventional MRI-guided radio-frequency thermal ablation of prostate cancer," *IEEE Transactions on Medical Imaging*, vol. 22, no. 4, 2003.

[14] S. Gill, P. Abolmaesumi, and S. Vikal, "Intraoperative prostate tracking with slice-to-volume registration in MR," *International Conference of the Society for Medical Innovation and Technology*, pp. 154–158, 2008.

[15] H. Tadayyon, S. Vikal, S. Gill, A. Lasso, and G. Fichtinger, "MRI-Guided prostate motion tracking by means of multislice-to-volume registration," vol. 7625. SPIE Medical Imaging, 2010.

[16] E. Canto, H. Singh, S. Shariat, D. Kadmon, B. Miles, T. Wheeler, and K. Slawin, "Effects of systematic 12-core biopsy on the performance of percent free prostate specific antigen for prostate cancer detection," *Journal of Urology*, vol. 172, pp. 900–904, 2004.

[17] B. Fei, C. Kemper, and D. L. Wilson, "Three-dimensional warping registration of the pelvis and prostate," vol. 4684. SPIE, 2002.

[18] H. Tadayyon, A. Lasso, S. Gill, A. Kaushal, P. Guion, and G. Fichtinger, "Target motion compensation in MRI-guided prostate biopsy with static images." 32nd Annual International IEEE EMBS Conference, 2010.

[19] A. Krieger, R. Susil, C. Menard, J. A. Coleman, G. Fichtinger, E. Atalar, and L. Whitcomb, "Design of a novel MRI compatible manipulator for image guided prostate interventions," *IEEE Transactions on Biomedical Engineering*, vol. 52, no. 2, 2005.

[20] B. Fei, A. Wheaton, and Z. L. et al., "Automatic MR volume registration and its evaluation for the pelvis and prostate," *Physics in Medicine and Biology*, vol. 47, pp. 823 – 838, 2002.

[21] N. Hansen, "The CMA evolution strategy: A comparing," *Springer*, pp. 75–102, 2006.

[22] A. Lasso, S. Avni, and G. Fichtinger, "Targeting error simulator for image-guided prostate needle placement." 32nd Annual International IEEE EMBS Conference, 2010.

[23] J. Hensel, C. Mnard, P. Chung, and et al., "Development of multiorgan finite element-based prostate deformation model enabling registration of endorectal coil magnetic resonance imaging for radiotherapy planning," *International Journal of Radiation Oncology * Biology * Physics*, vol. 68, pp. 1522–1528, 2007.

[24] M. Zhang, R. Alhajj, and J. Rokne, "Effectiveness of optimal incremental multi-step nearest neighbor search," *Expert Systems with Applications*, vol. 37, no. 8, pp. 6018 – 6027, 2010.